ACS APPLIED MATERIALS & INTERFACES

www.acsami.org

Research Article

Quench-Type Electrochemiluminescence Immunosensor Based on Resonance Energy Transfer from Carbon Nanotubes and Au-Nanoparticles-Enhanced g-C_3N_4 to CuO@Polydopamine for Procalcitonin Detection

Cui Song, Xiaojian Li, Lihua Hu,* Tengfei Shi, Dan Wu, Hongmin Ma, Yong Zhang, Dawei Fan, Qin Wei,* and Huangxian Ju

Cite This: *ACS Appl. Mater. Interfaces* 2020, 12, 8006–8015

Read Online

ACCESS | Metrics & More | Article Recommendations | Supporting Information

ABSTRACT: A new type of sandwich electrochemiluminescence (ECL) immunosensor dependent on ECL resonance energy transfer (ECL-RET) to achieve sensitive detection of procalcitonin (PCT) has been designed. In brief, carbon nanotubes (CNT) and Au-nanoparticles-functionalized graphitic carbon nitride (g-C_3N_4−CNT@Au) and CuO nanospheres covered with polydopamine (PDA) layer (CuO@PDA) were synthesized and applied as ECL donor and receptor, respectively. g-C_3N_4−CNT nanomaterials were in situ prepared on the basis of $\pi-\pi$ conjugation, and the CNT content in the composite were optimized to achieve a strong and stable ECL signal. At the same time, Au nanoparticles were used to functionalize g-C_3N_4−CNT to further increase the ECL intensity and the loading amount of primary antibody (Ab_1). Moreover, CuO@PDA was first used to successfully quench the ECL signal of g-C_3N_4−CNT@Au. Under the optimum experimental conditions, the linear detection range for PCT concentration was within 0.0001−10 ng mL^{-1} and the detection limit was 25.7 fg mL^{-1} (S/N = 3). Considering prominent specificity, reproducibility, and stability, the prepared immunosensor was used to assess recovery rate of PCT in human serum according to the standard addition method and the result was satisfactory. In addition, it is worth mentioning that a novel ECL-RET pair of g-C_3N_4−CNT@Au (donor)/CuO@PDA (acceptor) was first developed, which offered an effective analytical tool for sensitive detection of biomarkers in early disease diagnostics.

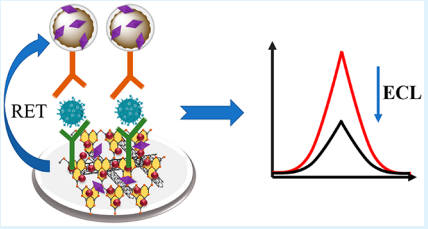

KEYWORDS: *electrochemiluminescence, resonance energy transfer, g-C_3N_4−CNT, CuO nanosphere, procalcitonin*

1. INTRODUCTION

Recently, more than 210 000 patients worldwide have been dying from sepsis every year.[1] In the serum of patients with sepsis, the concentration of procalcitonin (PCT) will increase as the disease progresses, but the concentration of procalcitonin in healthy individuals is very low.[2−4] Therefore, procalcitonin is considered to be a representative biomarker for the diagnosis of sepsis.[5,6] Sensitive detection of PCT in the human body has important significance for early prevention of sepsis. So far, only a few methods have been invented to accomplish the detection of PCT, such as radioimmunoassay,[7] colloidal gold colorimetry,[8,9] and microfluidic immunoassay.[10] Nevertheless, the above methods have some limitations, such as long detection time or narrow detection range. Therefore, it is still urgent to explore new methods with the advantage of a rapid, simple, wide detection range and ultrasensitivity for detection of PCT.

Electrochemiluminescence (ECL) as a new emerging product of the combination of electrochemistry and chemiluminescence is favored by many researchers in food analysis, bioanalysis, and environmental pollution analysis because it has lower background noise, a wider linear range, and more convenient operation.[11−13] Graphitic carbon nitride (g-C_3N_4) is an attractive nanomaterial with a p-conjugated graphite plane,[14−16] which has broad application because of its nontoxicity, chemical stability, and excellent optical and electrical properties.[17−19] In addition, the ECL performance of g-C_3N_4 attracted the attention of scholars for its high quantum yields.[20,21] However, the poor conductivity of g-C_3N_4 semiconductor resulted in an unstable and weak ECL signal. So researchers have chosen different kinds of materials, such as polyaniline[22] and β-cyclodextrin[23] to functionalize g-C_3N_4 to improve its ECL performance. The multiwalled carbon nanotube (CNT) as one typical carbon nanomaterial has a unique structure, excellent electrical conductivity, and high specific surface area, which have been a research hot spot for many years.[24−26] However, few research studies investigating the influence of CNT on the ECL emission of g-C_3N_4 have

Received: December 17, 2019
Accepted: January 23, 2020
Published: January 23, 2020

https://dx.doi.org/10.1021/acsami.9b22782
ACS Appl. Mater. Interfaces 2020, 12, 8006–8015

Scheme 1. Preparation Process of the g-C_3N_4−CNT@Au and CuO@PDA-Ab_2 Conjugate and Fabrication Process of the Proposed PCT Immunosensor

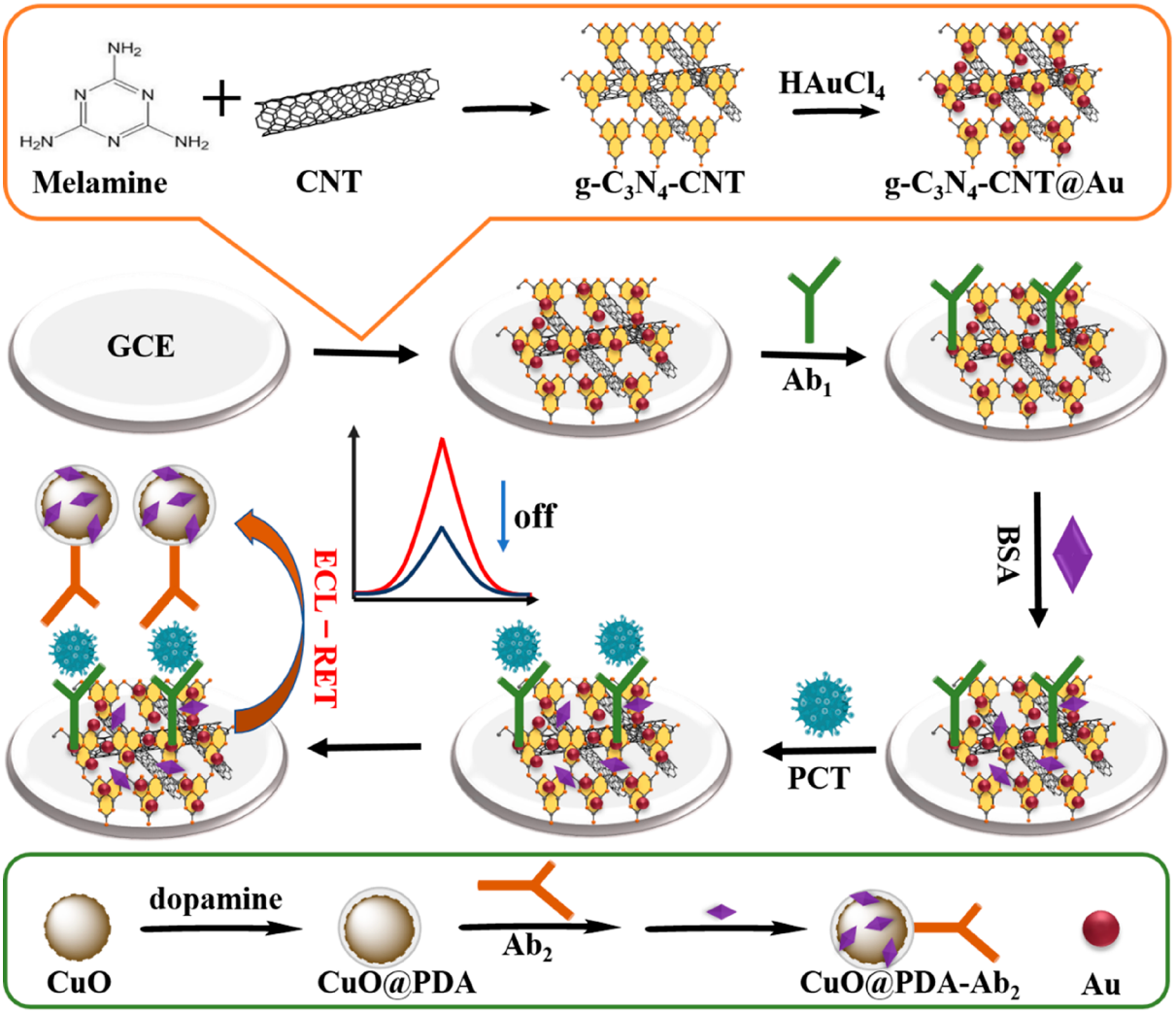

been reported. Herein, on the basis of the excellent conductivity of CNT, g-C_3N_4−CNT composite material was synthesized and used to enhance the ECL strength and stability of g-C_3N_4. In addition, Au nanoparticles with perfect biocompatibility and electron-transfer capabilities are frequently used to fabricate biosensors.[27−29] Thus, we also load Au nanoparticles onto g-C_3N_4−CNT to stabilize electron transfer and payload antibodies so as to further improve biosensor stability and sensitivity.

Herein, considering the superior ECL performance of the newly designed g-C_3N_4−CNT@Au, a sandwich-type immunosensor dependent on the resonance energy transfer (RET) between g-C_3N_4−CNT@Au and CuO nanospheres covered by polydopamine has been fabricated for the first time. In this work, CuO was prepared and first applied as a suitable RET acceptor on account of its high stability, nontoxicity, low cost, and high surface area.[30,31] In addition, the ultraviolet adsorption spectrum of the prepared CuO nanosphere was found to effectively cover the ECL emission spectrum of g-C_3N_4. So CuO could quench the ECL emission of g-C_3N_4 donor through energy dissipation in the CuO acceptor.[32,33] Polydopamine (PDA) is widely used in biosensing and biomedical fields because of its attractive biocompatibility, strong adhesion, and ease of functionalization.[34−36] The dopamine hydrochloride salt was self-polymerized onto the CuO surface to form a polydopamine shell, which could improve the biocompatibility of CuO and increase the loading of antibodies.

On the basis of the above analysis, a quenching-type ECL immunosensor dependent on energy resonance transfer from g-C_3N_4−CNT@Au to CuO@PDA was first constructed for PCT detection. g-C_3N_4−CNT@Au exhibited stronger and more stable ECL signal than pure g-C_3N_4. Moreover, when CuO@PDA was introduced into the biosensor, the ECL intensity was significantly reduced, indicating that CuO@PDA was suitable for ECL quenching. In addition, the fabricated biosensor realized the detection range within 0.0001−10 ng mL^{-1} of PCT and the detection limit was 25.7 fg mL^{-1}. On the basis of the above, the proposed strategy in this study can offer a new reference for sensing analysis of biomarkers.

2. EXPERIMENTAL SECTION

2.1. Synthesis of g-C_3N_4−CNT@Au. g-C_3N_4−CNT was typically synthesized by the following procedures. Melamine (500 mg) and CNT (5 mg) were fully ground in a mortar. The obtained mixture was calcined for 4 h at 550 °C directly in the air of a muffle furnace to generate a blocky blue-gray g-C_3N_4−CNT powder, which was then fully ground. Next, the g-C_3N_4−CNT powder was dissolved in 100

https://dx.doi.org/10.1021/acsami.9b22782
ACS Appl. Mater. Interfaces 2020, 12, 8006−8015

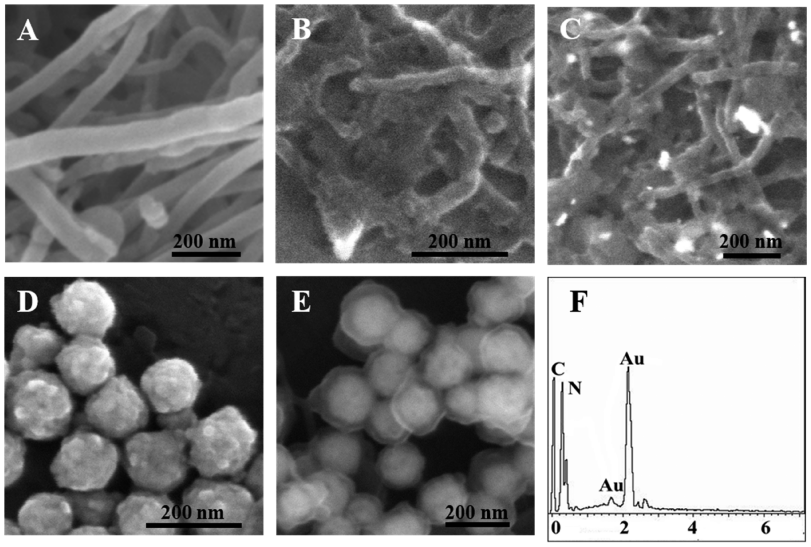

Figure 1. SEM images of CNT (A), g-C_3N_4–CNT (B), g-C_3N_4–CNT@Au (C), CuO (D), and CuO@PDA (E). EDX of g-C_3N_4–CNT@Au (F).

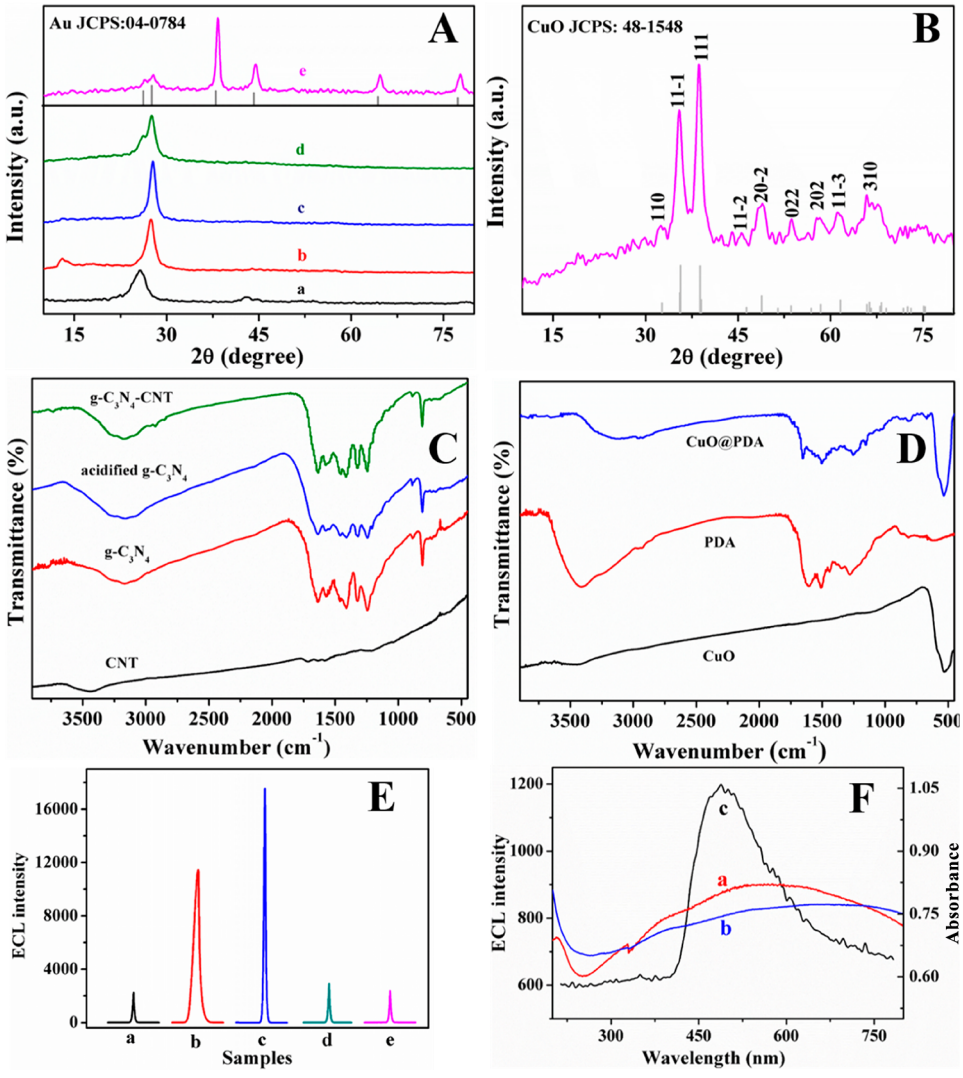

Figure 2. (A) XRD of CNT (a), g-C_3N_4 (b), acidified g-C_3N_4 (c), g-C_3N_4–CNT (d), and g-C_3N_4–CNT@Au (e). (B) XRD of CuO. (C) FT-IR spectra of CNT, g-C_3N_4, acidified g-C_3N_4, and g-C_3N_4–CNT. (D) FT-IR spectra of CuO, PDA, and CuO@PDA. (E) ECL intensity of g-C_3N_4/GCE (a), g-C_3N_4–CNT/GCE (b), g-C_3N_4–CNT@Au/GCE (c), CuO/g-C_3N_4–CNT@Au/GCE (d), and CuO@PDA/g-C_3N_4–CNT@Au/GCE (e). (F) UV–vis absorption of CuO (a) and CuO@PDA (b); the ECL emission spectra of g-C_3N_4 (c).

https://dx.doi.org/10.1021/acsami.9b22782
ACS Appl. Mater. Interfaces 2020, 12, 8006–8015

mL of HNO_3 (5 M) with ultrasound for 3 h at room temperature and refluxed at 125 °C for 24 h. Then the above product was centrifuged with ultrapure water at 9000 rpm for 5 min each time until its pH approached neutral. The obtained solid was vacuum-dried for 12 h at 55 °C. In addition, g-C_3N_4−CNT with different amounts of CNT were synthesized by reacting 1, 10, 20, and 50 mg of CNT with 500 mg of melamine, individually. As a control experiment, g-C_3N_4 and acid-treated g-C_3N_4 were similarly obtained according to the above process, but without the addition of CNT. Nanogold-decorated g-C_3N_4−CNT (denoted as g-C_3N_4−CNT@Au) was synthesized according to the literature with little modification.[37] Two percent $HAuCl_4$ (1.5 mL) and polyvinylpyrrolidone (K30; 5 mg) were added to a solution with 30 mg of g-C_3N_4−CNT dispersed in 20 mL of ultrapure water and stirred for 5 h. Subsequently, 2 mL of 50 mM sodium citrate along with a little $NaBH_4$ were slowly added to reduce $HAuCl_4$. After the solution reacted for 12 h in the dark, the solid was washed using ultrapure water three times (8500 rpm, 30 min) to remove free gold nanoparticles. Finally, the solid was vacuum-dried overnight at 55 °C to obtain g-C_3N_4−CNT@Au.

2.2. Preparation of CuO@PDA-Ab_2. CuO was synthesized according to the literature[38] and the detailed steps are given in the Supporting Information. As for the CuO@PDA core−shell nanospheres, 30 mg of CuO and 6 mg of dopamine were dispersed in 30 mL of pH 8.5 Tris-HCl (10 mmoL mL^{-1}) and stirred overnight. The CuO@PDA nanospheres were centrifugally washed with ultrapure water three times (8000 rpm, 5 min) to remove impurities. Finally, CuO@PDA nanospheres were dried for 12 h at 55 °C in vacuum.

The CuO@PDA-Ab_2 bioconjugates were prepared by adding 200 μL of PCT Ab_2 (10 μg mL^{-1}) to 2 mL of CuO@PDA (1 mg mL^{-1}) and the solution was incubated overnight at 4 °C. Then 100 μL of 0.1% bovine serum albumin (BSA) was added to occupy the nonspecific binding sites and the solid was centrifuged to remove extra reactants.[39] The obtained CuO@PDA-Ab_2 was dissolved in 2 mL of phosphate buffered saline (PBS, pH 7.4) and kept at 4 °C when not in use.

2.3. Construction of the Quench-Type ECL Immunosensor. The fabrication steps of the proposed PCT immunosensor are illustrated in Scheme 1. First, glassy carbon electrode (GCE, 4 mm in diameter) was first polished by Al_2O_3 powder (0.05 and 0.3 μm) until it became a smooth and clear mirror. Next, 6 μL of g-C_3N_4−CNT@Au was assembled on the surface of the GCE and dried at ambient temperature. After that, 6 μL of Ab_1 (10 μg·mL^{-1}) was linked to the above electrode surface via complexation between Au and NH_2 group. After the surface was gently rinsed with PBS (pH 7.4), 3 μL of BSA (0.1 wt %) was added to occupy the nonspecific recognition sites. After the surface was washed with PBS, 6 μL of different concentrations of PCT were coated onto the electrode surface and incubated for 1.5 h at 4 °C and carefully rinsed by PBS. Finally, 6 μL of CuO@PDA-Ab_2 was incubated onto the modified electrode surface. After the surface was washed with PBS, the quenching ECL immunosensor was constructed and kept at 4 °C before use.

2.4. ECL Detection. An ECL test was carried out in PBS (pH 7.4, 10 mL) containing 100 mM KCl and 80 mM $K_2S_2O_8$. The working potential was −1.2 to 0 V and the voltage of the photomultiplier tube (PMT) was set at 600 V with a scanning rate of 0.1 V s^{-1}.

3. RESULTS AND DISCUSSION

3.1. Characterization of the Used Nanomaterials. The morphology of the used materials was investigated by scanning electron microscopy (SEM). Representative images are shown in Figure 1. CNT showed a tubular structure and an aggregation state, and the pipe wall was smooth and almost electron-transparent (Figure 1A). However, after modification of g-C_3N_4, the g-C_3N_4 nanosheets covered or wrapped around the surface of the CNT through $\pi-\pi$ conjugation, which led to the formation of a rough surface in the g-C_3N_4−CNT (Figure 1B). The SEM image of g-C_3N_4−CNT@Au is presented in Figure 1C. A number of Au nanoparticles were dispersed on the outside of the g-C_3N_4−CNT composite. Also, the energy dispersive X-ray (EDX) result of g-C_3N_4−CNT@Au could also demonstrate the existence of Au nanoparticles in the g-C_3N_4−CNT@Au composites (Figure 1F). Figure 1D showed that the surface of the CuO nanospheres was rough, and the average diameter was around 160 nm. As shown in Figure 1E, PDA film was visibly coated on the surface of CuO to obtain CuO@PDA nanocomposite.

The wide-angle XRD patterns of the used materials are shown in Figure 2A,B. CNT displayed two obvious diffraction peaks at 25.74° and 43.39° (Figure 2A, curve a), which ascribed to the (002) and (100) crystal planes of the hexagonal graphite material, respectively (JCPDS card no. 41-1487). In addition, the peak at 13.04° corresponded to the (100) crystal plane, signifying the tri-s-triazine structure. The obvious peak at 27.41° can be ascribed to the (002) crystal plane, indicating the presence of a graphite-like interlayer stacking structure (Figure 2A, curve b). After acid treatment, the XRD pattern of the acidified g-C_3N_4 (Figure 2A, curve c) showed that the intensity of the (100) peak (13.16°) and (002) peak (27.65°) declined but the peak position was still close to that of g-C_3N_4, signifying that the lattice structure of g-C_3N_4 had not been destroyed after the acid treatment, which is good for construction of a biosensor. The XRD pattern of g-C_3N_4−CNT displayed in Figure 2A (curve d) shows two characteristic peaks at 26.16° and 27.52°, which can be assigned to CNT and g-C_3N_4 structure, respectively. This result proved the successful preparation of g-C_3N_4−CNT composite materials through a combination of CNT with g-C_3N_4. Moreover, as shown in g-C_3N_4−CNT@Au curve (Figure 2A, curve e), the appearance of peaks at 38.37° and 44.24° assigned to (111) and (200) planes of Au, respectively, verified the successful loading of Au nanoparticles onto the surface of the composites. Also, the XRD pattern in Figure 2B identified the successful preparation of monoclinic CuO (JCPDF 48-1548, Tenerife).

Figure 2C,D show the Fourier transform infrared (FT-IR) spectra of CNT, g-C_3N_4, acidified g-C_3N_4, g-C_3N_4−CNT, CuO, PDA, and CuO@PDA. In the CNT spectrum, the peak of the O−H stretch vibration appeared at 3140 cm^{-1}. The presence of carboxylic acid and carboxylate anion was verified by the peaks at 1706 and 1533 cm^{-1}.[40,41] In the g-C_3N_4 spectrum, a breathing vibration peak of the s-triazine ring appeared at 806 cm^{-1}.[42] Four peaks located at 1248, 1325, 1416, and 1570 cm^{-1} can be assigned to the typical stretching of C−N aromatic skeletal.[43] In addition, the peak at 1636 cm^{-1} was ascribed to the stretching vibration of C−N bond. The wider absorption band at around 3160 cm^{-1} corresponded to the stretching vibration of amino and hydroxyl group.[44] Compared to the original g-C_3N_4, the band strength at 3160 cm^{-1} of acidified g-C_3N_4 was stronger, which was due to the fact that the acidified g-C_3N_4 adsorbed more water molecule than bulk g-C_3N_4.[45] So acidified g-C_3N_4 showed good water solubility, which was beneficial for sensor construction. In the g-C_3N_4−CNT spectrum, the characteristic peaks of g-C_3N_4 were so strong that the adsorption peaks of CNT were overlapped. This can be explained by the low CNT content in the g-C_3N_4−CNT nanocomposite.

In the CuO spectrum, the peak at 524 cm^{-1} corresponded to the Cu−O stretch vibration, verifying the monoclinic structure of CuO.[46] Those peaks in the spectrum of PDA at 3430, 1642, 1430, and 1147 cm^{-1} were respectively attributed to the stretch vibration mode of O−H and N−H in the phenolic ring, the symmetric C−C stretching vibration, the bending vibration

https://dx.doi.org/10.1021/acsami.9b22782
ACS Appl. Mater. Interfaces 2020, 12, 8006−8015

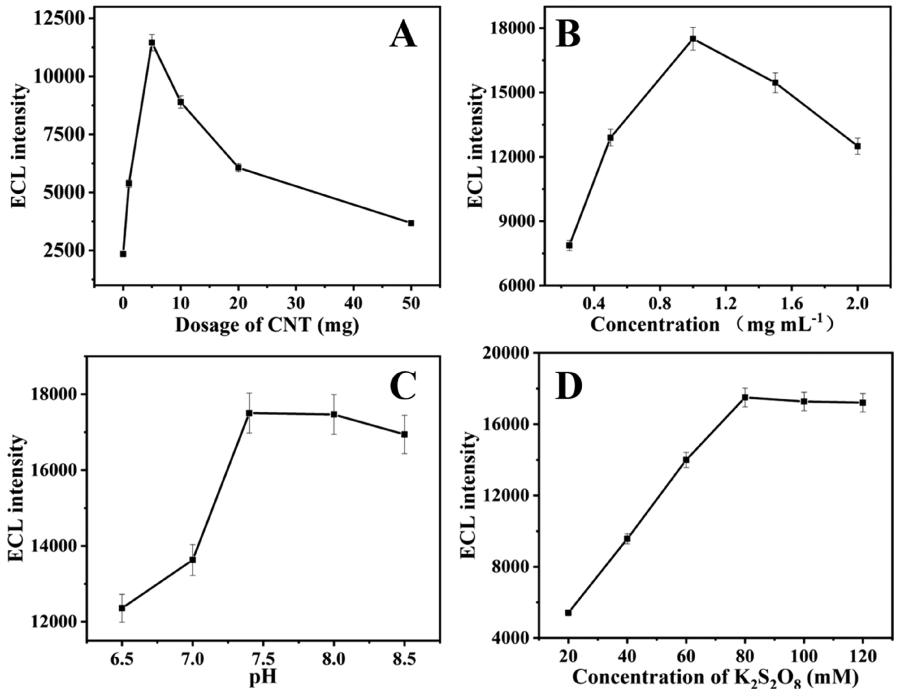

Figure 3. Effect of different doses of CNT (A), the concentration of g-C_3N_4−CNT@Au (B) and $K_2S_2O_8$ (D), pH (C) on the response of ECL intensity from g-C_3N_4−CNT@Au/GCE. Error bars = RSD (n = 3).

of phenolic C−O−H, and the heterocyclic N−H in-plane deformation breathing.[47] In the CuO@PDA spectrum, the characteristic peaks of CuO and PDA both appeared, which implied that PDA and CuO were combined successfully through the in situ polymerization of DA on the outside of the CuO nanoparticle.

3.2. ECL Emission Behavior of the g-C_3N_4−CNT@Au/$K_2S_2O_8$ System and Quenching Mechanism of CuO@PDA. In this work, the ECL signal amplification tactic was illustrated by control experiments. As depicted in Figure 2E, the emission signal of g-C_3N_4−CNT-modified electrode (curve b) was stronger than that of g-C_3N_4-modified electrode (curve a), proving that CNT could facilitate the ECL emission of g-C_3N_4 because the prominent electroconductibility of CNT accelerated the ECL redox reaction. Moreover, the ECL intensity of g-C_3N_4−CNT@Au-modified electrode (curve c) further increased. It was due to the fact that Au nanoparticles also had excellent conductivity, which can promote the transfer of electrons. The possible ECL mechanisms were discussed according to relevant reference reports.[48] When the electrode was scanned from −1.2 to 0 V, the g-C_3N_4 was first reduced to g-$C_3N_4^{\bullet-}$ (eq 1). Meanwhile, $S_2O_8^{2-}$ was reduced to $SO_4^{\bullet-}$ (eq 2). Then the strong oxidant $SO_4^{\bullet-}$ reacted with g-$C_3N_4^{\bullet-}$ to generate g-C_3N_4* (eq 3). Finally, an intense emission was released when g-C_3N_4* returned to the ground state from the excited state in the form of photons (eq 4).

$$\text{g-}C_3N_4 + e^- \rightarrow \text{g-}C_3N_4^{\bullet-} \quad (1)$$

$$S_2O_8^{2-} + e^- \rightarrow SO_4^{2-} + SO_4^{\bullet-} \quad (2)$$

$$\text{g-}C_3N_4^{\bullet-} + SO_4^{\bullet-} \rightarrow \text{g-}C_3N_4^{*} + SO_4^{2-} \quad (3)$$

$$\text{g-}C_3N_4^{*} \rightarrow \text{g-}C_3N_4 + h\nu \quad (4)$$

Meanwhile, the quenching effect of CuO (Figure 2E, curve d) and CuO@PDA (Figure 2E, curve e) toward the ECL emission of g-C_3N_4−CNT@Au was respectively investigated. It can be seen that both CuO and CuO@PDA can effectively quench the ECL emission of g-C_3N_4−CNT@Au. To study the possible quenching mechanism of CuO@PDA toward g-C_3N_4−CNT@Au, the UV−vis absorption spectra of CuO and CuO@PDA composites and the ECL emission spectrum of g-C_3N_4 were tested. The results depicted in Figure 2F show that the ECL emission range of g-C_3N_4 was about 400−650 nm (curve c). At the same time, the UV−vis spectra of CuO (curve a) and CuO@PDA (curve b) both showed a broader absorption range. An obvious overlap was observed between the ECL emission spectrum of g-C_3N_4 and the UV−vis absorption spectrum of CuO@PDA, making the RET process from the g-C_3N_4−CNT@Au (energy donor) to CuO@PDA (energy acceptor) possible.

3.3. Optimization of the Experimental Conditions. The CNT content in the g-C_3N_4−CNT nanocomposites was one of the important factors that affected the ECL property of the immunosensor. The ECL properties of six kinds of nanocomposites prepared by different doses of CNT were explored and the results are shown in Figure 3A. Corresponding detailed ECL response spectra are depicted in Figure S1 (Supporting Information). The ECL intensity reached the maximum at a 5 mg CNT dosage (Figure 3A). This can be explained as follows. In the g-C_3N_4−CNT nanocomposites, the g-C_3N_4 component is the luminescent material, but the poor conductivity of g-C_3N_4 semiconductor limits its ECL intensity; however, the CNT component with no or very weak ECL signal has good conductivity, which can enhance the ECL intensity of g-C_3N_4. As a result, the ECL signal increased continuously along with the increase of the CNT dose from 0 to 5 mg, which was due to the fact that the increased content of CNT endowed better conductivity of g-C_3N_4−CNT nanocomposites. However, a further increase of the CNT dosage from 5 to 50 mg resulted in a reduced ECL intensity. It could be due to the fact that as the content of CNT in the g-

https://dx.doi.org/10.1021/acsami.9b22782
ACS Appl. Mater. Interfaces 2020, 12, 8006−8015

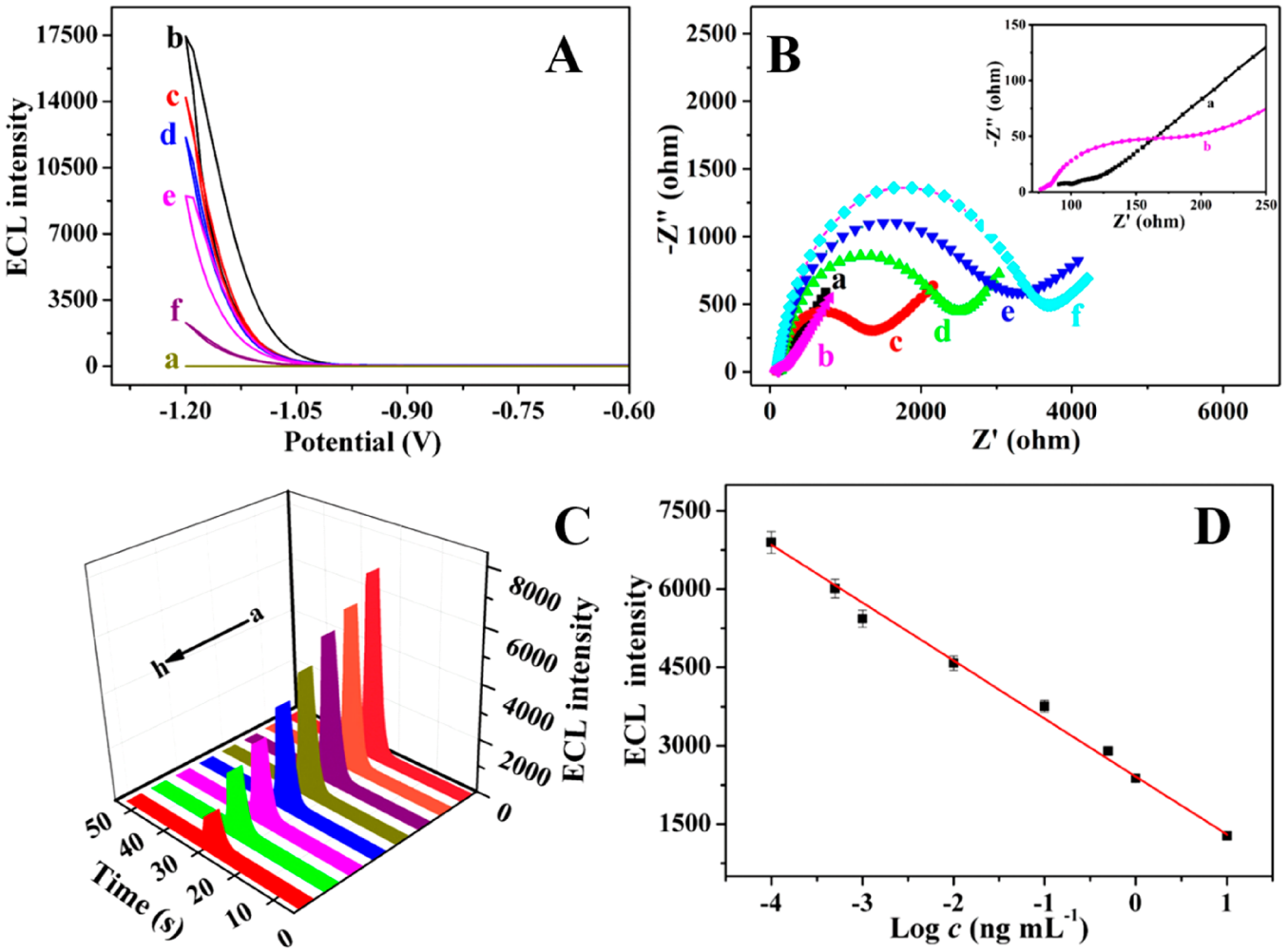

Figure 4. (A) ECL intensity−potential curves of GCE (a), g-C_3N_4/CNT@Au/GCE (b), Ab_1/g-C_3N_4−CNT@Au/GCE (c), BSA/Ab_1/g-C_3N_4−CNT@Au/GCE (d), PCT/BSA/Ab_1/g-C_3N_4−CNT@Au/GCE (e), and CuO@PDA-Ab_2/PCT/BSA/Ab_1/g-C_3N_4−CNT@Au/GCE (f) in PBS (pH 7.4) containing 80 mM $K_2S_2O_8$ and 0.1 M KCl. (B) Corresponding EIS in 2.5 mM $Fe(CN)_6^{3-/4-}$ and 0.1 M KNO_3. (C) ECL response of the immunosensor to different concentrations of PCT, from (a) to (h): 0.0001, 0.0005, 0.001, 0.01, 0.1, 0.5, 1, and 10 ng mL^{-1}. (D) Calibration curve of the immunosensor for different concentrations of PCT.

C_3N_4−CNT nanocomposites further increased, the excess CNT piled up with each other. This process could hinder the electron transfer and result in a weakening of the ECL signal. On the basis of the above, a 5 mg CNT dosage was chosen for the preparation of *g*-C_3N_4−CNT nanomaterials.

For the purpose of getting the best immunosensor performance, other experimental conditions were further optimized. Figure 3B exhibited the effect of different substrate concentrations on the ECL response of the biosensor. At the beginning, the ECL intensity was positively correlated with the concentration of g-C_3N_4−CNT@Au. When the concentration was above 1.0 mg mL^{-1}, the ECL intensity exhibited a sustained downward trend because the excessive substrate blocked the electron transmission. Consequently, 1 mg mL^{-1} was the optimum concentration of the g-C_3N_4−CNT@Au. As can be seen from Figure 3C, the corresponding emission intensity reached the maximum at pH 7.4. Thus, pH 7.4 was selected as the optimum condition. In addition, the concentration of the coreactant $K_2S_2O_8$ was also important for the ECL performance of g-C_3N_4−CNT@Au. As demonstrated in Figure 3D, the ECL signal strengthened with the increasing concentration of $K_2S_2O_8$ in detection solution and leveled off after 80 mM $K_2S_2O_8$. Thus, 80 mM $K_2S_2O_8$ was determined as the optimum concentration of the coreactant.

3.4. Characterization of the Immunosensor. To prove the successful fabrication of the proposed immunosensor, we investigated the relationship between ECL intensity and voltage during the construction process and displayed the results in Figure 4A, which were carried out under the best experimental conditions. The bare GCE showed a weak ECL (curve a), whereas g-C_3N_4−CNT@Au-modified electrode exhibited obvious ECL response (curve b). When Ab_1 (curve c), BSA (curve d), and PCT (curve e) were successively coated onto the electrode surface, the ECL intensity gradually decreased, which was due to the Ab_1, BSA, and PCT hindering the electron transfer. The electrode experienced a remarkable ECL inhibition after the decoration of the quenching probe of CuO@PDA-Ab_2 (curve f), verifying the high quenching efficiency of CuO@PDA-Ab_2.

The construction process of the biosensor was also verified through electrochemical impedance spectroscopy (EIS) tested at differently modified electrodes. The equivalent circuit for EIS was provided in Figure 4B, and their relevant data, which were simulated by ZSimPWin software, are listed in Table S1 (Supporting Information). As demonstrated in Figure 4B, the

https://dx.doi.org/10.1021/acsami.9b22782
ACS Appl. Mater. Interfaces 2020, 12, 8006−8015

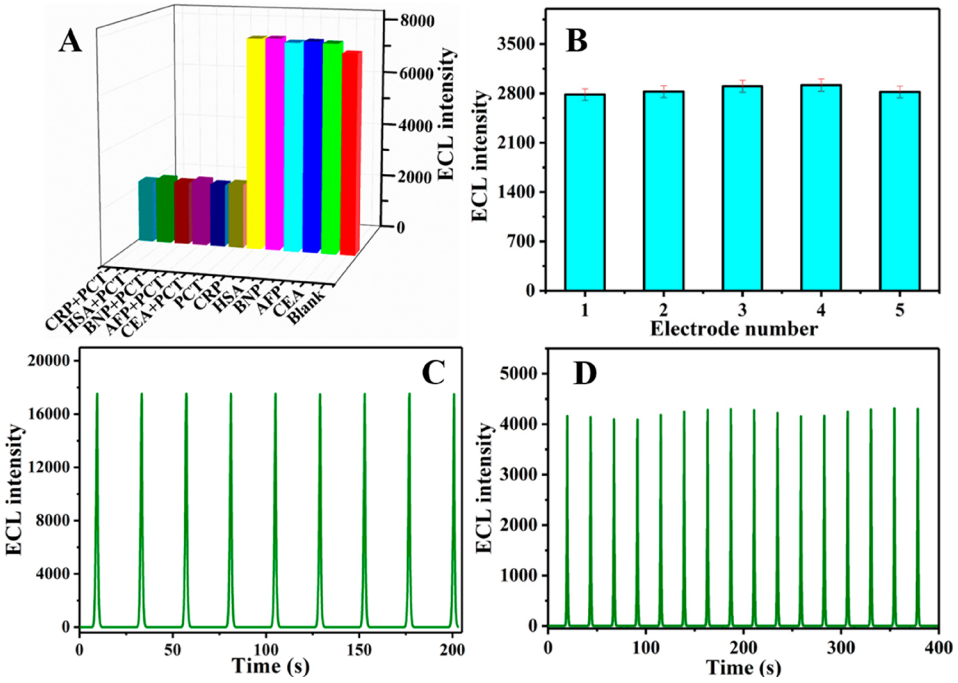

Figure 5. (A) Selectivity of the proposed ECL immunosensor in order: blank, CEA (1 ng mL^{-1}), AFP (1 ng mL^{-1}), BNP (1 ng mL^{-1}), HSA (1 ng mL^{-1}), CRP (1 ng mL^{-1}), PCT (1 ng mL^{-1}), and the mixture (containing CEA (100 ng mL^{-1}), AFP (100 ng mL^{-1}), BNP (100 ng mL^{-1}), HSA (100 ng mL^{-1}), CRP (100 ng mL^{-1}), and PCT (1 ng mL^{-1}). (B) Interassay study of the ECL immunosensor with 1 ng mL^{-1} PCT. Error bars = RSD (n = 3). (C) Stability of g-C_3N_4−CNT@Au/GCE in pH 7.4 PBS containing 80 mM $K_2S_2O_8$ and 0.1 M KCl. (D) Stability of ECL intensity under continuous scanning for 16 cycles in PBS (pH 7.4) containing 80 mM $K_2S_2O_8$ and 0.1 M KCl for detection of 10 pg mL^{-1} PCT.

diameter of the semicircle, which was related to the electron-transfer resistance (R_{et}) at the electrode−solution interface, represented the restricted diffusion of the redox probe $[Fe(CN)_6]^{3-/4-}$ accessing the modified layers on the electrode. The EIS curve of bare GCE was nearly a straight line (curve a), which was ascribed to the fact that the electron-transfer process was almost free,[49] whereas the curve of the working electrode modified with g-C_3N_4−CNT@Au displayed a small semicircle (curve b), indicating Au NPs and CNT endowed the substrate material with relatively favorable conductivity. After successive modification of Ab_1 (curve c), BSA (curve d), and PCT protein antigen (curve e), the semicircle diameter of the EIS was gradually increased, which was due to the fact that the Ab_1, BSA, and PCT proteins as nonelectroactive substances blocked the electron transfer. When the electrode was decorated with CuO@PDA-Ab_2, the hindrance of electron transfers further increased, resulting in the maximum R_{et} value (curve f) and proving the occurrence of the immunoreactions between Ag and Ab_2 bioconjugates. All the results above were consistent with the CV profiles in Figure S2, manifesting the successful construction of the quenching ECL immunosensor.

3.5. Analytical Performance of the Fabricated ECL Immunosensor. Different concentrations of PCT were tested to evaluate the sensing performance of the proposed immunosensor under the optimized experimental conditions. As shown in Figure 4C, the ECL intensity decreased along with the PCT concentration gradually increasing. The calibration curve in Figure 4D showed that ECL intensity versus the logarithm of PCT concentration was linear from 0.0001 to 10 ng mL^{-1}. The linear relation was I = 2412.1 − 1109.6 × lg c and the correlation coefficient was 0.994. The detection limit was 25.7 fg mL^{-1} (S/N = 3). Compared with other detection methods (Table S2), a wider detection range and a lower detection limit were realized here. The lower detection limit might be because of the remarkable ECL property of g-C_3N_4−CNT@Au and prominent quenching efficiency of CuO@PDA.

3.6. Selectivity, Reproducibility, and Stability of the Fabricated Immunosensor. To assess the specificity of the fabricated immunosensor, carcinoembryonic antigen (CEA), alpha fetoprotein (AFP), B-type natriuretic peptide (BNP), human serum albumin (HSA), and C-reactive protein (CRP) were chosen as possible interfering agents. First, PCT antigen of 1 ng mL^{-1} was selected as the reference, a mixture solution was prepared through mixing 1 ng mL^{-1} PCT with 100 ng mL^{-1} CEA, 100 ng mL^{-1} AFP, 100 ng mL^{-1} BNP, 100 ng mL^{-1} HSA, and 100 ng mL^{-1} CRP, respectively. As can be seen from Figure 5A, the ECL response of the immunosensor constructed by the mixed solution was nearly the same as that by 1 ng mL^{-1} PCT. Moreover, ECL responses of the immunosensor for 0 ng mL^{-1} PCT, 1 ng mL^{-1} CEA, 1 ng mL^{-1} AFP, 1 ng mL^{-1} BNP, 1 ng mL^{-1} HSA, and 1 ng mL^{-1} CRP were also investigated. The results indicated the prominent selectivity of the fabricated ECL immunosensor.

Prominent reproducibility is necessary for the practical application of the immunosensor, which was inspected by inter- and intra-assay precision. Five immunosensors were constructed for analyzing 1 ng mL^{-1} PCT in the same batch (Figure 5B). Then the same ECL immunosensors incubated with 1 ng mL^{-1} PCT were detected in five different batches (Figure S3). The RSD values of the intra- and interassay study were 2.01% and 1.13%, indicating that the immunosensor has good reproducibility.

Operating stability is crucial for practical application of the ECL sensor. First, the stability of g-C_3N_4−CNT@Au, which was cast onto the electrode surface, was detected via

https://dx.doi.org/10.1021/acsami.9b22782
ACS Appl. Mater. Interfaces 2020, 12, 8006−8015

consecutive cyclic potential scan for nine cycles. The ECL intensity shown in Figure 5C was quite stable and the RSD was 0.97%. Besides, ECL emission of the immunosensor for detecting 10 pg mL^{-1} of PCT under consecutive scanning potential for 16 cycles is displayed in Figure 5D, and the RSD was 1.75%. The results demonstrated that the ECL signals were reliable on the basis of the excellent stability of the proposed immunosensor.

3.7. Application in Real Samples of Human Serum. The standard addition method was used to conduct the recovery experiment in real samples of human serum to evaluate the feasibility of this ECL immunosensor in clinical PCT detection. The results listed in Table S3 show that the recovery was in the range of 94.0−110%,which demonstrated reliability and practicality of the proposed biosensor.

4. CONCLUSION

In brief, a sandwich-type ECL immunosensor dependent on ECL-RET in the g-C_3N_4−CNT@Au donor and CuO@PDA acceptor system was developed for sensitive detection of PCT. In the proposed system, g-C_3N_4−CNT@Au nanocomposite was first prepared and used as the emission substrate. For realization of high quenching efficiency, CuO@PDA was employed as the quenching probe via resonance energy transfer toward g-C_3N_4−CNT@Au. A wider linear detection range for PCT from 0.0001 to 10 ng mL^{-1} and a low detection limit of 25.7 fg mL^{-1} (S/N = 3) were achieved in this proposed strategy. The immunosensor exhibited prominent selectivity, reproducibility, and stability. So, the new sensing method may be applied to sensitive analysis of biological molecules in early disease diagnostics.

■ ASSOCIATED CONTENT

Supporting Information

The Supporting Information is available free of charge at https://pubs.acs.org/doi/10.1021/acsami.9b22782.

Materials; apparatus; preparation of CuO nanospheres; ECL signals of *g*-C_3N_4-CNT prepared by different ratios of melamine/CNT; simulation parameters of the equivalent circuit components; CV profiles of each modification step of the ECL immunosensor; intra-assay study of the ECL immunosensor; comparison of the performance of the proposed and referenced immunosensor for PCT detection; results of PCT determination in human serum; additional references (PDF)

■ AUTHOR INFORMATION

Corresponding Authors

Lihua Hu − *Collaborative Innovation Center for Green Chemical Manufacturing and Accurate Detection, School of Chemistry and Chemical Engineering and Key Laboratory of Interfacial Reaction & Sensing Analysis in Universities of Shandong, School of Chemistry and Chemical Engineering, University of Jinan, Jinan 250022, P.R. China;* orcid.org/0000-0002-4996-3372; Email: hulihua1206@163.com

Qin Wei − *Collaborative Innovation Center for Green Chemical Manufacturing and Accurate Detection, School of Chemistry and Chemical Engineering and Key Laboratory of Interfacial Reaction & Sensing Analysis in Universities of Shandong, School of Chemistry and Chemical Engineering, University of Jinan, Jinan 250022, P.R. China;* orcid.org/0000-0002-3034-8046; Email: sdjndxwq@163.com

Authors

Cui Song − *Collaborative Innovation Center for Green Chemical Manufacturing and Accurate Detection, School of Chemistry and Chemical Engineering and Key Laboratory of Interfacial Reaction & Sensing Analysis in Universities of Shandong, School of Chemistry and Chemical Engineering, University of Jinan, Jinan 250022, P.R. China*

Xiaojian Li − *Collaborative Innovation Center for Green Chemical Manufacturing and Accurate Detection, School of Chemistry and Chemical Engineering and Key Laboratory of Interfacial Reaction & Sensing Analysis in Universities of Shandong, School of Chemistry and Chemical Engineering, University of Jinan, Jinan 250022, P.R. China*

Tengfei Shi − *Collaborative Innovation Center for Green Chemical Manufacturing and Accurate Detection, School of Chemistry and Chemical Engineering and Key Laboratory of Interfacial Reaction & Sensing Analysis in Universities of Shandong, School of Chemistry and Chemical Engineering, University of Jinan, Jinan 250022, P.R. China*

Dan Wu − *Collaborative Innovation Center for Green Chemical Manufacturing and Accurate Detection, School of Chemistry and Chemical Engineering and Key Laboratory of Interfacial Reaction & Sensing Analysis in Universities of Shandong, School of Chemistry and Chemical Engineering, University of Jinan, Jinan 250022, P.R. China;* orcid.org/0000-0002-8732-5988

Hongmin Ma − *Collaborative Innovation Center for Green Chemical Manufacturing and Accurate Detection, School of Chemistry and Chemical Engineering and Key Laboratory of Interfacial Reaction & Sensing Analysis in Universities of Shandong, School of Chemistry and Chemical Engineering, University of Jinan, Jinan 250022, P.R. China;* orcid.org/0000-0002-7061-8944

Yong Zhang − *Collaborative Innovation Center for Green Chemical Manufacturing and Accurate Detection, School of Chemistry and Chemical Engineering and Key Laboratory of Interfacial Reaction & Sensing Analysis in Universities of Shandong, School of Chemistry and Chemical Engineering, University of Jinan, Jinan 250022, P.R. China;* orcid.org/0000-0002-5831-637X

Dawei Fan − *Collaborative Innovation Center for Green Chemical Manufacturing and Accurate Detection, School of Chemistry and Chemical Engineering and Key Laboratory of Interfacial Reaction & Sensing Analysis in Universities of Shandong, School of Chemistry and Chemical Engineering, University of Jinan, Jinan 250022, P.R. China*

Huangxian Ju − *Key Laboratory of Analytical Chemistry for Life Science, School of Chemistry and Chemical Engineering, Nanjing University, Nanjing 210023, P.R. China;* orcid.org/0000-0002-6741-5302

Complete contact information is available at: https://pubs.acs.org/10.1021/acsami.9b22782

Notes

The authors declare no competing financial interest.

■ ACKNOWLEDGMENTS

This study was supported by the National Key Scientific Instrument and Equipment Development Project of China (No. 21627809), National Natural Science Foundation of China (Nos. 21607055, 21675063, 21775054, 21505051, 21575050, 21777056, and 21427808).

REFERENCES

(1) Liu, F.; Xiang, G.; Yuan, R.; Chen, X.; Luo, F.; Jiang, D.; Huang, S.; Li, Y.; Pu, X. Procalcitonin Sensitive Detection Based on Graphene−Gold Nanocomposite Film Sensor Platform and Single-Walled Carbon Nanohorns/Hollow Pt Chains Complex as Signal Tags. *Biosens. Bioelectron.* **2014**, *60*, 210−217.

(2) Simon, L.; Gauvin, F.; Amre, D. K.; Saint-Louis, P.; Lacroix, J. Serum Procalcitonin and C-Reactive Protein Levels as Markers of Bacterial Infection: A Systematic Review and Meta-Analysis. *Clin. Infect. Dis.* **2004**, *39* (2), 206−217.

(3) Luzzani, A.; Polati, E.; Dorizzi, R.; Rungatscher, A.; Pavan, R.; Merlini, A. Comparison of Procalcitonin and C-reactive Protein as Markers of Sepsis. *Crit. Care Med.* **2003**, *31* (6), 1737−1741.

(4) Maruna, P.; Nedělníková, K.; Gürlich, R. Physiology and Genetics of Procalcitonin. *Physiol. Res.* **2000**, *49* (Suppl 1), S57−S61.

(5) Tsokos, M.; Reichelt, U.; Nierhaus, A.; Püschel, K. Serum Procalcitonin (PCT): A Valuable Biochemical Parameter for the Post-Mortem Diagnosis of Sepsis. *Int. J. Legal Med.* **2001**, *114* (4−5), 237−243.

(6) Reinhart, K.; Karzai, W.; Hartog-Schier, C. Procalcitonin (PCT) and Its Role in the Diagnosis of Sepsis. *Sepsis* **1998**, *2* (2), 157−161.

(7) Zhang, X.; Meng, H.; Sun, X.; Xu, L.; Zhang, L.; Shi, D.; Feng, X.; Lu, R.; Chen, Z. Elevation of Vitamin D-Binding Protein Levels in the Plasma of Patients with Generalized Aggressive Periodontitis. *J. Periodontal Res.* **2013**, *48* (1), 74−79.

(8) Wu, Y.; Liu, L.; Liang, Z.; Shen, Z.; Zhu, X. Colorimetric and Electrochemical Study on the Interaction Between Gold Nanoparticles and Unmodified DNA. *Curr. Nanosci.* **2011**, *7* (3), 359−365.

(9) Galetto-Lacour, A.; Zamora, S. A.; Gervaix, A. Bedside Procalcitonin and C-reactive Protein Tests in Children with Fever Without Localizing Signs of Infection Seen in A Referral Center. *Pediatrics* **2003**, *112* (5), 1054−1060.

(10) Shao, X.-Y.; Wang, C.-R.; Xie, C.-M.; Wang, X.-G.; Liang, R.-L.; Xu, W.-W. Rapid and Sensitive Lateral Flow Immunoassay Method for Procalcitonin (PCT) Based on Time-Resolved Immunochromatography. *Sensors* **2017**, *17* (3), 480.

(11) Wu, B.; Hu, C.; Hu, X.; Cao, H.; Huang, C.; Shen, H.; Jia, N. Sensitive ECL Immunosensor for Detection of Retinol-Binding Protein Based on Double-Assisted Signal Amplification Strategy of Multiwalled Carbon Nanotubes and Ru(bpy)32+ Doped Mesoporous Silica Nanospheres. *Biosens. Bioelectron.* **2013**, *50*, 300−304.

(12) Zeng, W.-J.; Liao, N.; Lei, Y.-M.; Zhao, J.; Chai, Y.-Q.; Yuan, R.; Zhuo, Y. Hemin as Electrochemically Regenerable Co-reaction Accelerator for Construction of An Ultrasensitive PTCA-Based Electrochemiluminescent Aptasensor. *Biosens. Bioelectron.* **2018**, *100*, 490−496.

(13) Wei, Y.; Wang, H.; Sun, S.; Tang, L.; Cao, Y.; Deng, B. An Ultrasensitive Electrochemiluminescence Sensor Based on Reduced Graphene Oxide-Copper Sulfide Composite Coupled with Capillary Electrophoresis for Determination of Amlodipine Besylate in Mice Plasma. *Biosens. Bioelectron.* **2016**, *86*, 714−719.

(14) Li, X.; Zhang, J.; Shen, L.; Ma, Y.; Lei, W.; Cui, Q.; Zou, G. Preparation and Characterization of Graphitic Carbon Nitride Through Pyrolysis of Melamine. *Appl. Phys. A: Mater. Sci. Process.* **2009**, *94* (2), 387−392.

(15) Zou, X.; Liu, M.; Wu, J.; Ajayan, P. M.; Li, J.; Liu, B.; Yakobson, B. I. How the Nitrogen-Doped Graphene Quantum Dots Catalyze Electroreduction of CO_2 to Tydrocarbons and Oxygenates. *ACS Catal.* **2017**, *7* (9), 6245−6250.

(16) Xiong, M.; Rong, Q.; Meng, H.; Zhang, X. Two-Dimensional Graphitic Carbon Nitride Nanosheets for Biosensing Applications. *Biosens. Bioelectron.* **2017**, *89*, 212−223.

(17) Ong, W.-J.; Tan, L.-L.; Ng, Y.-H.; Yong, S.-T.; Chai, S.-P. Graphitic Carbon Nitride ($g\text{-}C_3N_4$)-Based Photocatalysts for Artificial Photosynthesis and Environmental Remediation: Are We A Step Closer to Achieving Sustainability? *Chem. Rev.* **2016**, *116* (12), 7159−7329.

(18) Liu, Y.; Wang, R.; Yang, Z.; Du, H.; Jiang, Y.; Shen, C.; Liang, K.; Xu, A. Enhanced Visible-Light Photocatalytic Activity of Z-scheme Graphitic Carbon Nitride/Oxygen Vacancy-Rich Zinc Oxide Hybrid Photocatalysts. *Chin. J. Catal.* **2015**, *36* (12), 2135−2144.

(19) Shinde, S.-S.; Sami, A.; Lee, J.-H. Sulfur Mediated Graphitic Carbon Nitride/S-Se-Graphene as A Metal-Free Hybrid Photocatalyst for Pollutant Degradation and Water Splitting. *Carbon* **2016**, *96*, 929−936.

(20) Hu, S.; Ouyang, W.; Guo, L.; Lin, Z.; Jiang, X.; Qiu, B.; Chen, G. Facile Synthesis of $Fe_3O_4/g\text{-}C_3N_4$/HKUST-1 Composites as A Novel Biosensor Platform for Ochratoxin A. *Biosens. Bioelectron.* **2017**, *92*, 718−723.

(21) Jin, Y.; Kang, Q.; Guo, X.; Zhang, B.; Shen, D.; Zou, G. Electrochemical-Signal-Amplification Strategy for An Electrochemiluminescence Immunoassay with $g\text{-}C_3N_4$ as Tags. *Anal. Chem.* **2018**, *90* (21), 12930−12936.

(22) Zhao, Y.; Liu, Y.; Li, X.; Wang, H.; Zhang, Y.; Ma, H.; Wei, Q. Label-Free ECL Immunosensor for the Early Diagnosis of Rheumatoid Arthritis Based on Asymmetric Heterogeneous Polyaniline-Gold Nanomaterial. *Sens. Actuators, B* **2018**, *257*, 354−361.

(23) Wang, B.; Wang, H.; Zhong, X.; Chai, Y.; Chen, S.; Yuan, R. A Highly Sensitive Electrochemiluminescence Biosensor for the Detection of Organophosphate Pesticides Based on Cyclodextrin Functionalized Graphitic Carbon Nitride and Enzyme Inhibition. *Chem. Commun.* **2016**, *52* (28), 5049−5052.

(24) Bottini, M.; Bruckner, S.; Nika, K.; Bottini, N.; Bellucci, S.; Magrini, A.; Bergamaschi, A.; Mustelin, T. Multi-Walled Carbon Nanotubes Induce T Lymphocyte Apoptosis. *Toxicol. Lett.* **2006**, *160* (2), 121−126.

(25) Du, X.; Miao, Z.; Zhang, D.; Fang, Y.; Ma, M.; Chen, Q. Facile Synthesis of β-Lactoglobulin-Functionalized Multi-Wall Carbon Nanotubes and Gold Nanoparticles on Glassy Carbon Electrode for Electrochemical Sensing. *Biosens. Bioelectron.* **2014**, *62*, 73−78.

(26) Dehghani, M.-H.; Mostofi, M.; Alimohammadi, M.; Mckay, G.; Yetilmezsoy, K.; Albadarin, A.-B.; Heibati, B.; Alghouti, M.; Mubarak, N.-M.; Sahu, J.-N. High-Performance Removal of Toxic Phenol by Single-Walled and Multi-Walled Carbon Nanotubes: Kinetics, Adsorption, Mechanism and Optimization Studies. *J. Ind. Eng. Chem.* **2016**, *35*, 63−74.

(27) Gui, G.-F.; Zhuo, Y.; Chai, Y.-Q.; Xiang, Y.; Yuan, R. The Ru Complex and Hollow Gold Nanoparticles Branched-Hydrogel as Signal Probe for Construction of Electrochemiluminescent Aptasensor. *Biosens. Bioelectron.* **2016**, *77*, 7−12.

(28) Fan, Y.; Tan, X.; Ou, X.; Chen, S.; Wei, S. An Ultrasensitive Electrochemiluminescence Biosensor for the Detection of Concanavalin A Based on Au Nanoparticles-Thiosemicarbazide Functionalized PtNi Nanocubes as Signal Enhancer. *Biosens. Bioelectron.* **2017**, *87*, 802−806.

(29) Gai, Q.-Q.; Wang, D.-M.; Huang, R.-F.; Liang, X.-X.; Wu, H.-L.; Tao, X.-Y. Distance-Dependent Quenching and Enhancing of Electrochemiluminescence from Tris(2, 2′-bipyridine) Ruthenium (II)/Tripropylamine System by Gold Nanoparticles and Its Sensing Applications. *Biosens. Bioelectron.* **2018**, *118*, 80−87.

(30) Xu, L.; Su, J.; Zheng, G.; Zhang, L. Enhanced Photocatalytic Performance of Porous ZnO Thin Films by CuO Nanoparticles Surface Modification. *Mater. Sci. Eng., B* **2019**, *248*, 114405.

(31) Liang, Z.; Zhao, Z.; Sun, T.; Shi, W.; Cui, F. Enhanced Adsorption of the Cationic Dyes in the Spherical CuO/Meso-Silica Nano Composite and Impact of Solution Chemistry. *J. Colloid Interface Sci.* **2017**, *485*, 192−200.

(32) Lu, H.-J.; Pan, J.-B.; Wang, Y.-Z.; Ji, S.-Y.; Zhao, W.; Luo, X.-L.; Xu, J.-J.; Chen, H.-Y. Electrochemiluminescence Energy Resonance Transfer System Between RuSi Nanoparticles and Hollow Au Nanocages for Nucleic Acid Detection. *Anal. Chem.* **2018**, *90* (17), 10434−10441.

(33) Li, Z.; Lin, Z.; Wu, X.; Chen, H.; Chai, Y.; Yuan, R. Highly Efficient Electrochemiluminescence Resonance Energy Transfer System in One Nanostructure: Its Application for Ultrasensitive Detection of MicroRNA in Cancer Cells. *Anal. Chem.* **2017**, *89* (11), 6029−6035.

https://dx.doi.org/10.1021/acsami.9b22782
ACS Appl. Mater. Interfaces 2020, 12, 8006−8015

(34) Varghese Hansen, R.; Yang, J.; Zheng, L. Flexible Electrochromic Materials Based on CNT/PDA Hybrids. *Adv. Colloid Interface Sci.* **2018**, *258*, 21−35.
(35) Wang, Y.; Gu, F.-Q.; Ni, L.-J.; Liang, K.; Marcus, K.; Liu, S.-L.; Yang, F.; Chen, J.-J.; Feng, Z.-S. Easily Fabricated and Lightweight PPy/PDA/AgNW Composites for Excellent Electromagnetic Interference Shielding. *Nanoscale* **2017**, *9* (46), 18318−18325.
(36) Li, Y.; Shi, S.; Cao, H.; Zhao, Z.; Su, C.; Wen, H. Improvement of the Antifouling Performance and Stability of An Anion Exchange Membrane by Surface Modification with Graphene Oxide (GO) and Polydopamine (PDA). *J. Membr. Sci.* **2018**, *566*, 44−53.
(37) Zhuang, J.; Lai, W.; Xu, M.; Zhou, Q.; Tang, D. Plasmonic AuNP/g-C_3N_4 Nanohybrid-Based Photoelectrochemical Sensing Platform for Ultrasensitive Monitoring of Polynucleotide Kinase Activity Accompanying DNAzyme-Catalyzed Precipitation Amplification. *ACS Appl. Mater. Interfaces* **2015**, *7* (15), 8330−8338.
(38) Zhang, J.; Liu, J.; Peng, Q.; Wang, X.; Li, Y. Nearly Monodisperse Cu_2O and CuO Nanospheres: Preparation and Applications for Sensitive Gas Sensors. *Chem. Mater.* **2006**, *18* (4), 867−871.
(39) Li, X.; Wu, D.; Ma, H.; Wang, H.; Wang, Y.; Fan, D.; Du, B.; Wei, Q.; Zhang, N. Ultrasensitive Amyloid-β Proteins Detection Based on Curcumin Conjugated ZnO Nanoparticles Quenching Electrochemiluminescence Behavior of Luminol Immobilized on Au@MoS_2/Bi_2S_3 Nanorods. *Biosens. Bioelectron.* **2019**, *131*, 136−142.
(40) Bora, A.; Mohan, K.; Pegu, D.; Gohain, C.-B.; Dolui, S.-K. A Room Temperature Methanol Vapor Sensor Based on Highly Conducting Carboxylated Multi-Walled Carbon Nanotube/Polyaniline Nanotube Composite. *Sens. Actuators, B* **2017**, *253*, 977−986.
(41) Zheng, N.; Sun, W.; Liu, H.-Y.; Huang, Y.; Gao, J.; Mai, Y.-W. Effects of Carboxylated Carbon Nanotubes on the Phase Separation Behaviour and Fracture-Mechanical Properties of An Epoxy/Polysulfone Blend. *Compos. Sci. Technol.* **2018**, *159*, 180−188.
(42) Samsudin, M.-F.-R.; Bacho, N.; Sufian, S.; Ng, Y.-H. Photocatalytic Degradation of Phenol Wastewater Over Z-scheme g-C_3N_4/CNT/$BiVO_4$ Heterostructure Photocatalyst Under Solar Light Irradiation. *J. Mol. Liq.* **2019**, *277*, 977−988.
(43) Suryawanshi, A.; Dhanasekaran, P.; Mhamane, D.; Kelkar, S.; Patil, S.; Gupta, N.; Ogale, S. Doubling of Photocatalytic H_2 Evolution from g-C_3N_4 Via Its Nanocomposite Formation with Multiwall Carbon Nanotubes: Electronic and Morphological Effects. *Int. J. Hydrogen Energy* **2012**, *37* (12), 9584−9589.
(44) Chaudhary, D.; Vankar, V.-D.; Khare, N. Noble Metal-Free g-C_3N_4/TiO_2/CNT Ternary Nanocomposite with Enhanced Photocatalytic Performance Under Visible-Light Irradiation Via Multi-Step Charge Transfer Process. *Sol. Energy* **2017**, *158*, 132−139.
(45) Dong, F.; Zhao, Z.; Xiong, T.; Ni, Z.; Zhang, W.; Sun, Y.; Ho, W.-K. In Situ Construction of g-C_3N_4/g-C_3N_4 Metal-Free Heterojunction for Enhanced Visible-Light Photocatalysis. *ACS Appl. Mater. Interfaces* **2013**, *5* (21), 11392−11401.
(46) Erdoğan, İ.-Y.; Güllü, Ö. Optical and Structural Properties of CuO Nanofilm: Its Diode Application. *J. Alloys Compd.* **2010**, *492* (1−2), 378−383.
(47) Qian, Y.; Feng, J.; Fan, D.; Zhang, Y.; Kuang, X.; Wang, H.; Wei, Q.; Ju, H. A Sandwich-Type Photoelectrochemical Immunosensor for NT-pro BNP Detection Based on F-Bi_2WO_6/Ag_2S and GO/PDA for Signal Amplification. *Biosens. Bioelectron.* **2019**, *131*, 299−306.
(48) Li, X.; Zhang, X.; Ma, H.; Wu, D.; Zhang, Y.; Du, B.; Wei, Q. Cathodic Electrochemiluminescence Immunosensor Based on Nanocomposites of Semiconductor Carboxylated g-C_3N_4 and Graphene for the Ultrasensitive Detection of Squamous Cell Carcinoma Antigen. *Biosens. Bioelectron.* **2014**, *55* (2), 330−336.
(49) Shu, J.; Han, Z.; Zheng, T.; Du, D.; Zou, G.; Cui, H. Potential-Resolved Multicolor Electrochemiluminescence of N-(4-Aminobutyl)-N-Ethylisoluminol/Tetra(4-Carboxyphenyl)Porphyrin/TiO_2 Nanoluminophores. *Anal. Chem.* **2017**, *89* (23), 12636−12640.

https://dx.doi.org/10.1021/acsami.9b22782
ACS Appl. Mater. Interfaces 2020, 12, 8006−8015